Spectral Indices Survey for Oil Spill Detection in Coastal Areas

Ámbar Pérez-García, *Graduate Student Member, IEEE*, Adrián Rodríguez-Molina, Emma Hernández, and José Fco López

***Abstract*—When oil spills occur at sea, effective detection and monitoring are required to establish a successful response plan, and remote sensing emerges as an appropriate technology to support this process. Furthermore, Earth observation is progressively relying on low-cost multispectral sensors developed for monitoring particular features across various scenarios. However, despite these advancements, the ongoing challenge lies in reducing computational costs, resource requirements, and energy consumption. This work aims to select the spectral index that best detects coastal spills among those documented. The long-term goal is to develop a low-cost multispectral sensor with suitable bands. For this purpose, this study uses data from different sensors that acquired data of the Deepwater Horizon accident in the Gulf of Mexico. The confusion matrices, accuracy, and F1-score generated from the kNN pixel classification based on the indices values are measures of its performance. For this study, the recently introduced normalized difference oil index (NDOI) proves to be the best option for identifying coastal spills since it minimizes the false positives related to suspended sand and is quick to calculate. In addition, it has demonstrated that it helps distinguish different spill thicknesses and estimates the oil volume. Therefore, future research will focus on developing and validating a low-cost multispectral system that uses the NDOI bands to detect spills.**

***Index Terms*—Hyperspectral images (HSIs), oil spill, remote sensing (RS), spectral indices.**

I. Introduction

THE marine environment supports a diverse range of sea life that is extremely important for global biodiversity and quality of life, including climate regulation. Oil spills devastate marine and coastal environments, poisoning and suffocating marine wildlife, accumulating on the seafloor and beaches, and causing long-term environmental impacts. Remote sensing (RS) and spectral technology are valuable tools for monitoring oil spills and assessing clean-up. However, there are still limitations in processing speed and, therefore, response time. Spectral indices offer a swift response with minimal computational overhead, rendering them a valuable and efficient approximation. This comparative study is noteworthy as it assesses the performance of existing indices and explores their limitations, making it a valuable contribution to the field.

Tanker accidents, refineries, offshore platforms, and minor maritime operations produce tons of crude and oil products that reach the sea yearly [1]. The most common causes of spills are oil exploration, pipeline leaks, and crude oil transfer to tankers. Still, they are also caused by illegal oil extraction or natural causes such as earthquakes or hurricanes [2]. The conventional method for measuring marine pollution before the 1960s was to sail into polluted regions, take in situ measurements at different depths, and then examine them in laboratories to determine water properties. This way, precise results are obtained but at a high cost in terms of human and material resources. Besides, this approach is very time-consuming and is geographically limited due to the inability to survey broad areas [3]. Aircraft and coastguard forces were introduced to improve ocean surveillance. Simple photography and video at short distances are examples of this. However, data acquisition costs remain high for larger areas [4].

Satellite and aerial RS have proven to be adequate tools for detecting and mapping marine pollutants, providing valuable data for time-evolution modeling to track contaminants through space and time [3]. When monitoring large areas, satellites are more efficient than aircraft as they can cover more extensive regions. Hence, they are used to detect spills and lead to a timely response to the incident. Airborne sensors can then conduct exhaustive monitoring, quantify the scale of the disaster, and identify the type of pollutant [5]. In recent years, uncrewed aerial vehicles (UAVs) have become vital in RS, offering high flexibility and resolution for rapid real-time data collection, but face challenges like accurate geo-referencing and real-time processing of hyperspectral images [6]. Therefore, given its broad coverage, satellite monitoring emerges as the optimal choice for oil spill detection.

It is crucial to remember that not all sensors are equally effective because each spectral range has advantages and disadvantages for a specific scenario. Although synthetic aperture radar (SAR) sensors are frequently used for the detection of

Manuscript received 13 March 2024; revised 2 June 2024; accepted 30 July 2024. Date of publication 5 August 2024; date of current version 5 September 2024. The work of Ámbar Pérez-García was supported by "Agencia Canaria de Investigacion, Innovacion y Sociedad de la Informacion (ACIISI)" of the "Consejería de Universidades, Ciencia e Innovación y Cultura", the European Social Fund Plus (FSE+) "Programa Operativo Integrado de Canarias 2021-2027, Eje 3 Tema Prioritario 74 (85%)" under a predoctoral grant. The work of Adrián Rodríguez-Molina and Emma Hernández was supported by the "Vicerrectorado de Investigación y Transferencia de la Universidad de las Palmas de Gran Canaria" under a predoctoral grant during the research. We would also like to thank the TALENT-HExPERIA project, under contract PID2020-116417RB-C42, the PERSEO project, under contract CPP2021-008527, from "Programa de Colaboración Público-Privada" of "Gobierno de España", 2023-2025, and the OASIS-HARMONIE project, under contract PID2023-148285OB-C43 from "Proyectos de Generación de Conocimiento" 2023. *(Corresponding author: Ámbar Pérez-García.)*

The authors are with the Institute for Applied Microelectronics, University of Las Palmas de Gran Canaria, 35001 Las Palmas, Spain (e-mail: ambar.perez@ulpgc.es).

Digital Object Identifier 10.1109/JSTARS.2024.3438123

spillages, over the past decade, optical sensors have outperformed SAR in certain aspects of spill monitoring [7]. Part of this improvement is attributed to the proliferation of multispectral and hyperspectral sensors onboard satellites, which offer unprecedented spectral analysis of scenarios. Progress has also been made in developing low-cost multispectral sensors specialized in monitoring and characterizing a particular surface or features [8], [9], [10]. Optical sensors are a more suitable alternative than radar sensors for continuous monitoring due to their higher repetition time. This advantage stems from the greater presence of optical sensors onboard satellites, resulting in a higher repetition time for optical information from different sensors that can be combined. Optical sensor satellites guarantee a short revisit period, minutes for geostationary satellites, and a few hours for low Earth orbiting polar satellites. Instead, SAR satellites may require dozens of days to revisit midlatitude regions [11].

Multispectral and hyperspectral sensors can capture spectral signature-based 3-D images that provide valuable information about the composition of the surface studied in each pixel. A key feature in the optical detection of oil spills is that under sunglint, they might appear differently in shape, color, and contrast between light and dark [12]. The spectral signature of the spill varies with oil properties, the film thickness, its degree of evaporation, and the meteorological conditions such as sun illumination and air-water content [13]. It is possible to estimate the thickness of oil slicks with optical sensors [14]. Furthermore, due to their capacity to identify the chemical composition in detail and assess its abundance [15], high-spectral resolution sensors can differentiate false positives [5], distinguish oil types [16], [17], and quantify oil volume [18], [19], [20].

Several studies involve machine learning and neural networks (NNs) on high-precision maritime pollution detection with optical and radar sensors [21], [22], [23]. Although some AI methods discriminate between oil-contaminated and nonpolluted regions [24], [25], they are slower than performing a few mathematical operations such as spectral indices. The simplicity, dimensional reduction of the data to be processed, and the calculation speed of spectral indices are significant advantages over machine learning techniques. Furthermore, implementing spectral indices into hardware acceleration devices like graphics processing units (GPUs) and field programmable gate arrays (FPGAs) allows for parallel operations, further reducing processing time and energy consumed. Spectral indices become vital for monitoring in quasi-real-time, especially when working with hyperspectral sensors with hundreds of bands, and a short response time is required, for example, in a spill accident at sea [26].

The Deepwater Horizon (DWH) event-related hyperspectral and multispectral data are the focus of this investigation. The DWH oil spill, also known as the Gulf of Mexico oil spill, started on April 20, 2010, and discharged 780 000 m^3 of oil into the northern Gulf of Mexico for nearly three months [27]. When a spill such as the DWH happens, affecting a large coastal area and lasting for months, response teams cannot efficiently assess and contain all the damage. Thus, RS is crucial in decision-making. The long duration of the DWH event allowed scientists to collect data from a wide range of platforms and sensors, varying from SAR to optical sensors in the visible and thermal ranges, including multispectral and hyperspectral sensors, both onboard satellites and aircraft [28]. Thus, DWH marked a turning point in developing techniques and algorithms for oil spill monitoring and response.

This work arises from the interest in developing a low-cost multispectral sensor to monitor oil spills along coastlines. Based on the spectral indices, the sensor can be designed with just the essential bands, considerably decreasing cost and enhancing the accessibility of this technology. Therefore, this study aims to select the most suitable spectral index to build such a sensor. For this purpose, a survey of the spectral index documented in the literature that can identify oil spills at sea is presented, along with a section on the distinction of spill thickness and oil volume based on prior works. Due to the difficulty of accessing regions of the ocean contaminated by an oil spill, the cost associated with measuring it, and the hence, they are used to detect spills and rapidly change the event, obtaining ground truth for the images above is challenging. Therefore, relevant pixels are carefully hand-picked from the image and labeled with the region to which they belong. The recently introduced normalized difference oil index (NDOI) [29] has given the best results of the study, with an overall accuracy of 94.5%, and has proven valuable in differentiating oil-in-water spill thicknesses and volume.

II. State of the Art of Spectral Indices for Oil Spill Detection

Solar radiation travels through the atmosphere before it is reflected on Earth's surface and reaches the sensor. Therefore, optical RS produces images from the radiation emerging from the Earth's surface-atmosphere system in the direction of observation of the sensor. The intensity of the radiant flux for a given surface and a given wavelength is a physical quantity measured in watts per squared meter steradian $(W/(sr.m^2))$. As this quantity is susceptible to atmospheric disturbances, reflectance—defined as the ratio of the emitted surface flux to the incident flux—obtained after atmospheric correction is used [30]. The spectral reflectance signatures help to distinguish the targets because each material reflects and absorbs light differently for each wavelength. The interaction between electromagnetic waves and water depends on the optical properties of water, absorption, and scattering, which alter its reflectance. This response—captured by remote sensors—is strongly linked to the concentrations, types, and presence of substances in water [31]. RS is crucial in monitoring spills at sea. Hyperspectral sensors with superior spectral and spatial resolution facilitate the discrimination of false positives, and the identification of oil type [32]. However, the high dimension of the hyperspectral and multispectral images complicates their storage and processing. Furthermore, the high correlation of bands decreases the efficiency and accuracy of its analysis and classification [33]. The most relevant bands for the study are selected to solve this data volume problem.

Spectral indices are combinations of bands by simple arithmetic operations to highlight some spectral behavior and suppress the background. The band choice depends on the spectral

TABLE I
MOST CITED INDICES FOR IDENTIFYING SPILLS

Index	Equation	Measured property	Author
NDOI	$(R_{599}$ - $R_{870})/(R_{599}$ + $R_{870})$	Oil fluorescent characteristics	[29]
RAI	(Blue - IR) / (Blue + IR) $\sqrt{\sum_{i=1}^{N} b_i{}^2}$	Oil fluorescent characteristics	[36]
FI	(Blue - Red) / (Blue + Red)	Oil fluorescent characteristics	[36]
HI	$(\lambda_{1729} - \lambda_{1705})\dfrac{R_{1741} - R_{1705}}{\lambda_{1741} - \lambda_{1705}} + (R_{1705} - R_{1729})$	Oil-affected soils	[37]
OSI	$(DN_{\lambda_{Red}} - DN_{\lambda_{Yellow}})/(\lambda_{Red} - \lambda_{Yellow})$	Existence of crude oil	[38]
WAF	$(R_{1343} + R_{1563})/2 - R_{1453}$	Seawater characteristics	[39]
CDOM	R_{565}/R_{660}	Seawater characteristics	[40]
CHL	$log(max(R_{433,490,510})/R_{555})$	Surface chlorophyll a	[41]
NDVI	(NIR - Red) / (NIR + Red)	Live green vegetation	[42]
NDWI	$(R_{860} - R_{1240})/(R_{860} + R_{1240})$	Vegetation liquid water	[43]
Ratio B_2/B_{11}	Blue / R_{1614}	Oil presence	[44]

characteristics of the phenomenon under study. Oil spills can be found using a variety of thoroughly tested spectral indices. However, new and improved indices have recently been proposed that can be adapted to a specific satellite sensor image or a specific scene [34]. The pixel misclassification due to sand suspension on the coast is a weakness identified in most spectral indices in the literature [35]. Misclassification is a significant obstacle when spills occur in coastal areas. It makes the initial study of the oil spill, its follow-up, and the analysis of its long-term impact more difficult. Consequently, the NDOI—a new index that can mitigate this impact—was introduced [29].

The spectral index family commonly used to detect spills (see Table I) includes fluorescence index (FI) [36], rotation-absorption index (RAI), where b is the pixel radiance for the image band, [36], hydrogen index (HI) [37], and oil slope index (OSI) [38]. Seawater and vegetation indices are also included, such as water absorption feature (WAF) [39] and colored dissolved organic matter (CDOM) [40], or chlorophyll content (CHL) [41], normalized difference vegetation index (NDVI) [42], and normalized difference water index (NDWI) [43]. Band ratios are spectral indices where only two bands are used, partially normalizing the effect of clouds and shadows. Band ratios were born to improve the delineation accuracy provided by single-band pixels. This study will also use a custom ratio designed from Sentinel 2 bands to distinguish between polluted and clean water: ratio B_2/B_{11} [44]. Note that the wavelengths of the indices will not match exactly on all sensors, nor will it be possible to obtain all indices on all sensors due to the spectral ranges of each sensor. As airborne visible infrared imaging spectrometer (AVIRIS) covers the short-wave infrared (SWIR) range, it is possible to calculate spectral indices that are not possible with other sensors: HI, WAF, NDWI, and the ratio B2/B11.

Three types of spills can be distinguished spectrally by thickness: thin-film spills, thick-film spills, and emulsions (mixing of oil and seawater). Below 50 microns, the spots appear metallic, rainbow, or silver in color and are called sheens [45]. Thin-film oil has a yellow–orange hue and appears in the vicinity of thick-film oil slicks, which is usually the result of its dispersion. These spots are typically discontinuous and irregular. They are generally between 50 and 200 microns thick. The color of crude oil, dark reddish-brown or black, is visible in thick-film spills [46]. These spots are commonly continuous and compact, with a thickness above 200 microns. Finally, emulsions are water-to-oil mixtures with a red-orange color that appear in the convergence zones of the waves and look like long, narrow bands of oil [47]. Its thickness is difficult to measure precisely but is higher than that of the thick-film oil, exceeding 500 microns.

As mentioned in Section I, although there are several limitations to detecting spills with optical imaging, its potential and applicability are indisputable [44]. In the case of shallow water spills, thin-film spills exhibit the same spectral behavior as the ocean floor [48]. However, in the open sea, it is easier to distinguish the optical characteristics of crude oil. Seawater influences thin oil films (sheens) due to its near translucency. On the contrary, the transparency of thick oil slicks is weak, so their spectra are weakly affected by seawater. Therefore, the hydrocarbon spectral indices (NDOI, FI, RAI, HI, and OSI) help identify emulsions and continuous thick slicks. By contrast, the water and vegetation spectral indices (WAF, CDOM, CHL, NDVI, and NDWI) are more suitable for detecting sheens and seawater [45]. Both are complementary, so their combination improves recognition accuracy. In general, sheens are more easily noticed at viewing directions near the sun-glint zone, while thick films are more likely to be identified at viewing angles away from the sun [49].

Oil weathering processes act on the spills produced on the sea surface, causing their spreading, evaporation, dissolution, emulsion, etc., thus, modifying the volume of oil in the slick. Processes such as evaporation remove much of the volatile parts, but emulsification of the spill with seawater can increase the oil volume [50]. This article uses the Bonn Agreement Oil Appearance Code [51], adopted as a standard method for assessing the volume of oil in water in 2004. It codes the thickness of the slicks

TABLE II
CHARACTERISTICS OF THE STUDY'S SENSORS

Parameter	AVIRIS	HICO	MERIS
Spatial resolution Revisit period	20 m-1 m –	90 m 3 days	300 m 3 days
Spectral range	VNIR-SWIR	VNIR	VNIR
(nm)	366–2496	353–1080	412–900
Bandwidth	$<$10 nm	$\sim$ 6 nm	10 nm
Number of bands	224 bands	128 bands	15 bands
Band units	Radiance	L1B	TOA reflectance
Operational	1992–today	2009–2014	2002–2012
Platform	Airborne	ISS	Envisat Satellite
Organization	NASA JPL	ONR and NASA	ESA

from 1-5 in order of increasing thickness for sheens (silver/gray), rainbow, metallic, discontinuous, and continuous true oil colors. The Bonn Agreement Oil Appearance Code does not provide a specific code for emulsions due to their thickness variability and, therefore, volume estimation complexity [51]. Oil sheens have a thickness between 0.04 and 0.3 microns, rainbow-colored slicks between 0.3 and 5.0 microns, metallic-looking slicks are typically between 5.0 and 50 microns, and discontinuous true-color oil slicks can reach up to 200 microns. Thicker thicknesses fit into continuous true-color oil slicks or emulsions, depending on how degraded the oil is by mixing with water.

III. MATERIALS AND METHODS

A. Datasets

In this work, two images from each sensor—AVIRIS, Hyperspectral Imager for the Coastal Ocean (HICO), and Medium Resolution Imaging Spectrometer (MERIS)—have been used to contrast the results of the spectral indices. Table II shows their technical characteristics.

The AVIRIS is an airborne instrument that measures upwelling spectral radiance in 224 contiguous bands at 10 nm intervals across a wavelength range from 366 to 2496 nm (VNIR and SWIR) [52]. NASA's Jet Propulsion Laboratory (JPL) designed and built the sensor in California. Data are available from 1992 to the present. The main objective of the AVIRIS project is to identify, measure, and monitor constituents of the Earth's surface and atmosphere based on molecular absorption and particle scattering signatures [53]. It has flown in four different aircraft. The width, length, and spatial resolution of the recorded images vary with the flight altitude of the vehicle. For example, when flying at an altitude of 20 km, scenes of 11 km in width and 800 km in length are obtained with a spatial resolution of 20 m. The HICO is the first space-borne imaging spectrometer designed to sample the coastal ocean. It was developed by the Naval Research Laboratory (NRL) for the Office of Naval Research (ONR) and later cofunded by NASA's International Space Station (ISS) Program. It was operational between 2009 and 2014. Its purpose was to provide data for coastal scientific research worldwide. The instrument can obtain 2000 scenes each year with a revisit period of approximately three days. HICO has 120 bands between 380 and 960 nm (VNIR) sampled at 5.7 nm, with a spatial resolution of 90 m and a high signal-to-noise ratio

Fig. 1. Geolocation of survey images in the Gulf of Mexico (source: Google Earth V 9.147.0.2).

to resolve the complexity of the coastal ocean [54]. This work uses images with an L1B (sensor units) processing level.

The MERIS was a programmable spectrometer on the European Space Agency (ESA) Envisat mission. Its primary goal was to measure the color of the ocean, although atmospheric and land surface studies were also carried out. MERIS was developed under the leadership of ALCATEL Space Industries and was in operation from 2002 to 2012. One of its most outstanding features was the programmability of its spectral bands in width and position, with 15 bands between 412 and 900 nm and a bandwidth of 10 nm. The images are in top-of-atmosphere (TOA) reflectance units, with a spatial resolution of up to 300 m and a revisit time of around three days [55].

B. Study Area

The DWH oil rig was in the Gulf of Mexico, 93 km southeast of the Mississippi River Delta. When it exploded, a considerable volume of crude oil leaked out [56]. Fig. 1 shows the area covered by each of the images in the study to give the reader an idea of the dimensions of the different sensors. The oil spill studied was between 26° and 30° north and 84° and 92° west. We concentrate exclusively on the region of the image that is of the utmost concern, as the oil spill presents all the characteristics that we consider relevant to the study. Given that this is a dynamic process, we have provided the dates and times of image acquisition (see Table III).

The selected set of images contains thick and thin oil spills to test the effectiveness of the spectral indices against slicks of different characteristics and thicknesses. It is important to note that most of the water surrounding the spillage contains a small part of diluted oil. The whole surface close to the thick stains suffers from this contamination. As this is a near-shore spill, some scenes also show sand suspended in the ocean. We have masked out the clouds in the images following a methodology proposed by [57] that allows us to ensure accurate cloud masking tailored to the specific characteristics of our images.

In the AVIRIS scenes (see Fig. 2), the oil can be seen with the naked eye in the RGB composition. In the image captured on May 17, different thicknesses of oil slicks can be distinguished, with several bright lines running across the bottom half of the

TABLE III
DATE OF THE CAPTURE OF THE STUDY IMAGES

Image	Date	Acquisition (UTC)	Image reference name
AVIRIS 1	May 17	20:46	$f100517t01p00r11$
AVIRIS 2	May 18	19:59	$f100518t01p00r11$
HICO 1	May 24	14:55	$H2010144145510$
HICO 2	May 28	13:21	$H2010148132130$
MERIS 1	April 26	15:56	$ENV\_ME\_2\_FRG\_\_20100426T155651\_20100426T160013\_\_\_\_\_0202\_088\_498\_\_\_DSI\_R\_NT\_\_$
MERIS 1	May 02	16:08	$ENV\_ME\_2\_FRG\_\_20100502T160817\_20100502T161126\_\_\_\_\_0188\_089\_083\_\_\_DSI\_R\_NT\_\_$

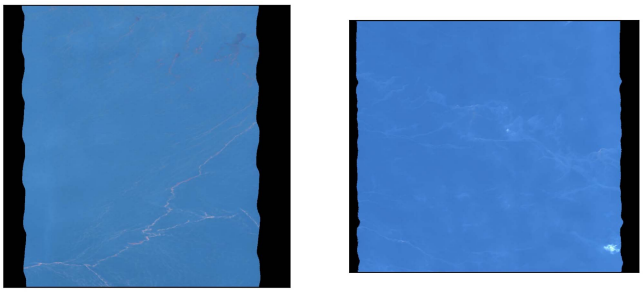

(a) (b)

Fig. 2. AVIRIS true color RGB images from 17 May 2010, at 20:46 and 18 May 2010, at 19:59. (a) AVIRIS 1. (b) AVIRIS 2.

(a) (b)

Fig. 3. HICO true color RGB images from 24 May 2010, at 14:55 and 28 May 2010, at 13:21. (a) HICO 1. (b) HICO 2.

figure, which correspond to an emulsion. There are also thick oil stains, seen as dark reddish rounded spots in the upper part of the image. In the May 18 image, traces of thin oil are faintly visible in a diagonal direction. There is also a tiny cloud in the lower right part. From now on, the AVIRIS image of 17 May 2010, will be called AVIRIS 1, and that of 18 May 2010, will be AVIRIS 2.

Regarding HICO images (see Fig. 3), in HICO 1, the one corresponding to May 24, the trail of sand in suspension from the Louisiana coast, specifically from the Mississippi River mouth, can be seen on the left side. On the right side of the image, there is also a faint vertical line of oil. In HICO 2, the one taken on May 28, practically no element can be seen, only the clouds in the bottom left corner.

Unlike the scenes shown, MERIS images cover a much larger land area at the cost of losing spatial resolution. The two images of Fig. 4—MERIS 1 and MERIS 2—cover the entire spill. In addition, both show different thicknesses of oil and part of the Mexican coastline. Thus, measuring the affected area and the thickness of the oil film at each point is more complicated. To highlight the spill-affected region effectively, we have masked

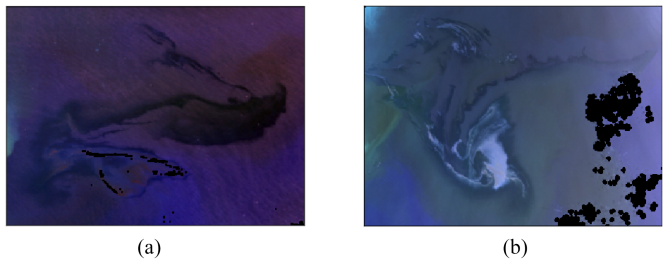

(a) (b)

Fig. 4. MERIS false color RGB images from 26 April 2010, at 15:56 and 2 May 2010, at 16:08. (a) MERIS 1. (b) MERIS 2.

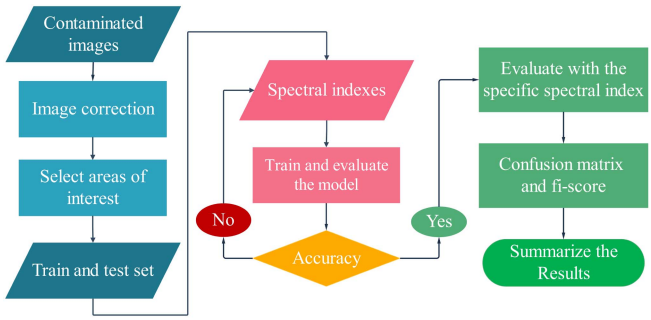

Fig. 5. Flowchart of the experimental process. Blue indicates the initial phase of data preparation, pink represents the algorithm's training phase, and green denotes the final phase of analysis and presentation of results. The yellow diamond indicates a decision point.

the clouds and the coastline in the image since they exhibit higher reflectivity values than the oil spill area. Both MERIS scenes are affected by sunglint and are thus displayed in a false RGB to facilitate the differentiation of the polluting material. These present an opportunity to explore indices' behavior and performance under sunglint.

It is interesting to note the rapid dispersal of the spill, deduced from its shape change between 26 April and 2 May. These underline how crucial it is that the clean-up teams and maritime authorities take immediate action.

C. Experimental Process

Fig. 5 provides a flowchart to facilitate the explanation of the experimental procedure. The process has three stages: the preprocessing of the images, the data processing and training of the computational model, and the result evaluation. Once the AVIRIS, HICO, and MERIS images have been selected and downloaded from the corresponding platforms [53], [54], [55], these must be corrected using the information provided in the

image metadata. If necessary, cloud masks are applied. Next, we select the areas of interest from the true-color or false-color images and, create the subsets train (70%) and test (30%) randomly. Although it is not possible to distinguish thicknesses in all the scenes, it is essential to ensure that all three subsets contain different thicknesses of oil slicks and are different from each other to obtain a consistent sample.

We employed the bands of the multispectral and hyperspectral images to calculate the corresponding spectral indices for oil detection and seawater composition. For each spectral index, pixels of the interest areas are extracted and used to train and test the computational kNN model. The kNN algorithm [58], [59] is a popular nonparametric classification method known to have significant classification performance and simple implementation. One of the keys to the success of this algorithm is the hyperparameter k, which allows the selection of the number of neighbors that influence the classification of a given pixel. Different values of k have been tested for the dataset, finding that from k equal to five, the improvement in the accuracy of the indices is insignificant. This method is efficient in classification problems with imbalanced class distributions, a situation in which our scenario is found, given that there are many more water pixels than spill pixels [60]. Combining the index's visual analysis with the calculation of model errors makes it possible to establish which are most effective in each scenario.

The confusion matrices produced by the classification, combined with its corresponding accuracy, F1-score metrics, and a figure of merit, γ, will be used to calculate the error. A confusion matrix illustrates the relationship between predicted and real labels, enabling assessing the classification model's quality. Accuracy is one of the most widely used and favored metrics in classification. It measures the percentage of correct predictions [61]. Moreover, the F1-score is particularly useful with uneven class distribution, giving more importance to smaller classes [62]. Finally, we introduce a figure of merit denoted as γ, which combines the results of the previous metrics

$$\gamma = \text{Accuracy} \cdot \frac{F1^{\text{Oil}}}{F1^{\text{Water}}} \tag{1}$$

where Accuracy is the overall accuracy [61], and $F1^{\text{Oil}}$ and $F1^{\text{Water}}$ denote the F1-scores [62] for the oil and water classes, γ encompasses the error metrics by weighing the accuracy with the ratio between the F1-scores of the oil and water classes. This approach enables γ to account for accuracy relative to the performance of unbalanced classes.

D. Validation

Oil spills at sea vary rapidly due to the movement of currents that disperse the oil and evaporation processes. These circumstances mean that measuring the composition and thickness of spillage in situ in all affected areas is complicated and costly in terms of time and resources. For these reasons, there is often no ground truth of spills against which to test the results of spectral indices and classification algorithms. We propose a technique to validate them based on the Bonn Agreement Oil Appearance Code [51]. To address the lack of ground truth, we hand-pick the pixels that belong to a class, label them, and shuffle them to build a training and test dataset with a sample ratio of 70/30. Second, we use the two sets to train the kNN algorithm and validate its result. These will provide a measure of the effectiveness of the indices. Although the kNN introduces a small error in the classification, the primary importance lies in the indices. So, if the values of a spectral index for a class are similar but different from other classes, we will achieve satisfactory results in the confusion matrix and error metrics.

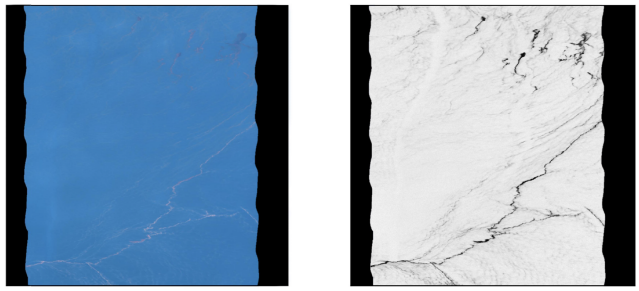

(a) (b)

Fig. 6. AVIRIS true color RGB and NDOI from 17 May 2010, at 20:46. (a) AVIRIS 1. (b) NDOI.

The validation technique has been used both for evaluating the effectiveness of the indices and for verifying the performance of NDOI in estimating thicknesses and volumes of oil spills. For this purpose, two previous works will be taken as a reference [20], [45]. The authors estimated the thickness and oil volume with AVIRIS and MERIS imagery on dates close to those used in this work. Based on these results as the ground truth, we conducted tests to evaluate the effectiveness of the validation method and the spectral index's capability to estimate the oil spill's thickness and volume. The detailed results and analysis are presented in Section IV-D.

IV. Experimental Results and Discussion

First, we performed a visual examination of the NDOI about the RGB representation for the representative image of each sensor to illustrate the index characteristics found in previous work [29], [35]. Next, we extend the study by performing a qualitative analysis of spectral indices from the literature for several scenes. Then, its performance is quantified using metric confusion matrices, precision, and F1-score. Finally, we test whether the NDOI can distinguish different thicknesses and volumes of oil at sea.

A. NDOI Qualitative Analysis

The first scene to be studied (see Fig. 6) is AVIRIS 1. This image is of great interest because it shows spots of different thicknesses. The naked eye can see how the NDOI index perfectly highlights the emulsion, which is noticeable in the RGB image as a narrow orange band of spill across it. It also reveals the thicker oil slicks, which can be observed in RGB as dark red-brown spots, although the darker part is not adequately identified. Thinner, discontinuous areas typically produced by the dispersion of an emulsion or thick patches are near them in a

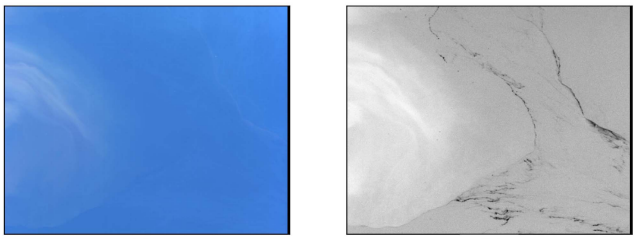

(a) (b)

Fig. 7. HICO true color RGB and NDOI from 24 May 2010, at 14:55. (a) HICO 1. (b) NDOI.

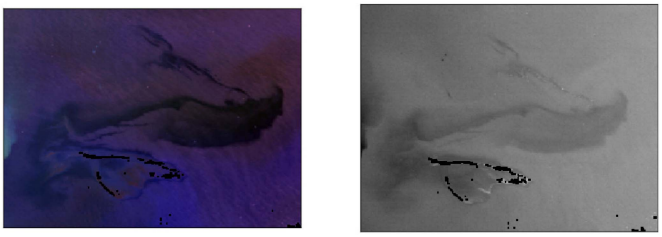

(a) (b)

Fig. 8. MERIS false color RGB and NDOI from 26 April 2010, at 15:56. (a) MERIS 1. (b) NDOI.

softer tone. Fine stains appear as a faint, yellowish color in RGB, making them more difficult to discern. Thinner spots, known as sheens, are not detectable with the index—nor are they visible in RGB, as these are semitransparent, usually acquiring a metallic, rainbow, or silver color. It is worth noting that most of the ocean surface surrounding the spills is somehow tainted. Almost the entire surrounding region, unhighlighted by the spectral index (white color), is covered by a thin layer of oil. Because the spectral index can detect several different thicknesses in the AVIRIS image (emulsion, thick spot, and thin spot), it is to be expected that the NDOI can help infer spill thickness in a subsequent scene.

Apart from distinguishing the thickness of the spot, a crucially important aspect of a spectral index is its ability to discriminate look-alikes. As mentioned in Section II, most indices in the literature highlight the suspended sand as if it were part of the spill. This is a handicap in the study of coastal discharges. Fig. 7 shows HICO 1, where it is possible to identify sand from the delta produced by the Mississippi River on the left side. The NDOI index completely dismisses this suspended sand and accentuates the thin strands of the spill to the right of it. Thus, with this spectral index, the oil pathways are clearly defined.

Finally, it is relevant to underline how efficiently the index performs when treating the entire spill. When a slick of this magnitude is involved, the situation is often quite complex. Its characteristics can be subject to variations related to ocean currents or the composition of the water in which it travels. Although the new index does not highlight all the observable details in the false-color image (see Fig. 8), it indicates the thicker spill and the trajectories followed by the thinner spill strips. In this case, it is difficult to identify the complete slick using spectral indices due to its wide variety of spectral behavior and the sunglint. However, NDOI can detect different mixtures of oil and seawater, which is intricately linked to the volume of oil (further explored in Section IV-D). More elaborate post-processing could be performed to classify regions of different characteristics. At first glance, the novel index distinguishes between three classes. The filament is highlighted in white, corresponding to an emulsion zone. The thick spill is marked in dark gray, and the sea in light gray. The following sections will test whether sunglint affects the ability of the indices to differentiate water from oil and to identify their characteristics.

Because the advanced synthetic aperture radar (ASAR) sensor is also on board the Envisat mission, it was possible to compare the data generated by the radar with the outcomes of the NDOI for MERIS in earlier work [35]. NDOI is said to be robust because its pattern matches the ASAR radar image captured on the same day.

Given the results, the implementation of the NDOI index is broadly satisfactory. We must now compare its effectiveness with the other spectral indices in the literature.

B. NDOI: A Comparative Study

Starting again with AVIRIS 1, Fig. 9 shows a compilation of the literature indices and the RGB image. At first glance, most indices present a similar pattern to that observed in NDOI. Specifically, both RAI, FI, and CDOM seem identical to NDOI. While RAI highlights fine oil slicks less than NDOI, CDOM enhances them more than NDOI. The B2/B11 ratio accurately detects the presence of oil, even highlighting areas with very thin spill thickness. The NDVI exhibits a similar structure to NDOI, though not as pronounced in the sheens. However, the index is inverted, highlighting the unpolluted area. Similarly, the HI and OSI are inverted. These indices only point to the thickest spill zone, the emulsions. The HI index shows banding because it involves AVIRIS bands with wavelengths longer than 1700 nm, in which the signal-to-noise ratio is poor. The WAF and NDWI indices also indicate the thicker regions of the spill. Only the emulsions are identified in the WAF case, whereas, in the case of NDWI, slightly thinner discharges are also discernible. Very thick spill parts that turn dark red or almost black have different spectral behavior and are difficult for the spectral indices to distinguish, except for NDWI and the B2/B11 ratio. Finally, the chlorophyll index, CHL, is the least clear. The emulsion's narrow lines are visible, and the thick spill spots are highlighted in white. However, the rest of the scene seems blurred, so the remaining oil is indistinguishable. It is possible that all indices are valid in certain aspects but are not equally efficient and do not provide the same results for different thickness.

Some indices cannot be determined with HICO since this sensor does not reach the shortwave infrared range: HI, WAF, NDWI, and ratio B2/B11. The most noticeable difference between the spectral indices shown in HICO 1 (see Fig. 10) is how they treat the suspended sand from the delta. As explained before, NDOI discards this sand completely, and the oil path is clearly defined, with two thin lines splitting the image. NDVI presents the same behavior but again inverted. The subsequent index with similar behavior is RAI. However, the two oil

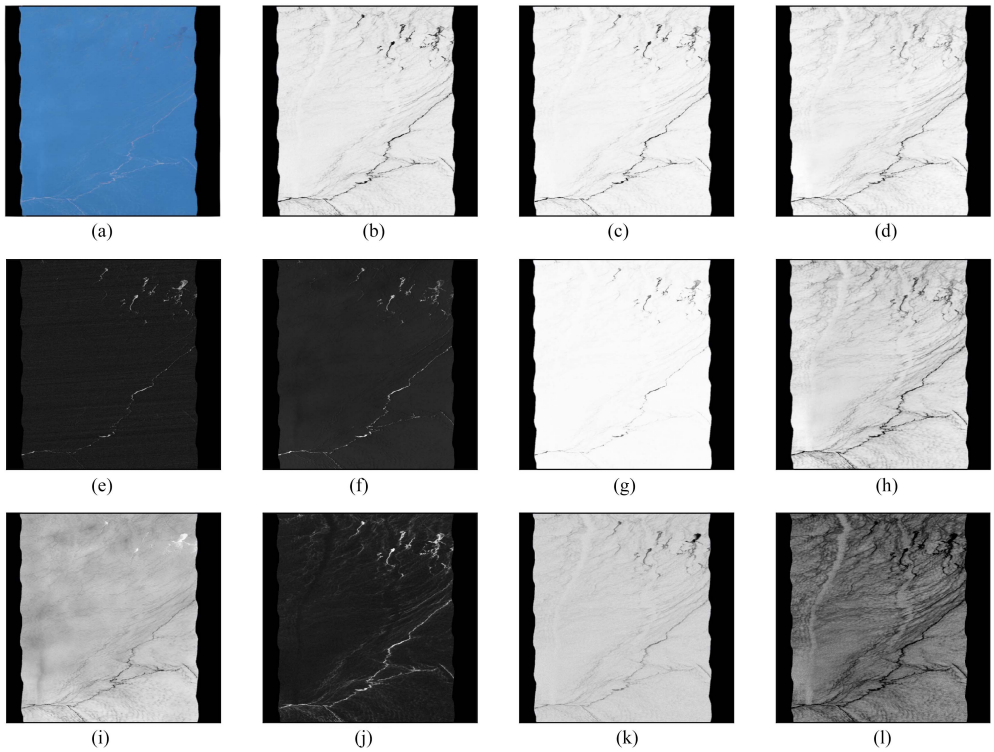

Fig. 9. AVIRIS true color RGB and spectral indices from 17 May 17 at 20:46. (a) RGB AVIRIS 1. (b) NDOI. (c) RAI. (d) FI. (e) HI. (f) OSI. (g) WAF. (h) CDOM. (i) CHL. (j) NDVI. (k) NDWI. (l) RATIO B2/B11.

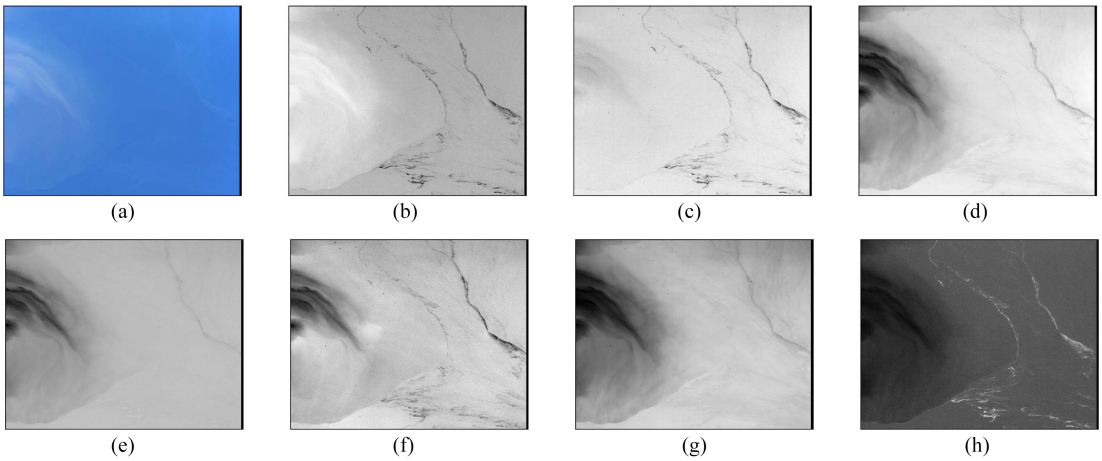

Fig. 10. HICO true color RGB and spectral indices from 24 May 2010, at 14:55. (a) RGB HICO 1. (b) NDOI. (c) RAI. (d) FI. (e) OSI. (f) CDOM. (g) CHL. (h) NDVI.

filaments are not as well defined, and some of the suspended sand could be mistaken for a sheen. The remaining indices mistakenly highlighted the sand in suspension as a spill. For CDOM, the line of the oil spill farthest from the delta can be seen, and the closer one can be intuited. For FI and CHL, just the most distant line from the mouth of the river can be distinguished. In the case of OSI, the oil spill is practically indistinguishable, with only the sand in suspension standing out.

As for HICO, MERIS does not cover the shortwave infrared. Consequently, HI , WAF, NDWI, and ratio B2/B11 cannot be applied either. Since MERIS images cover the entire spill and the sunglint effect, some spectral behaviors in the image differ significantly from others, making analysis more challenging. Guided by the false-color composition in MERIS 1 (see Fig. 11), two oil cores appear in the discharge. One is at the lower left of the image (principal), and the other is centered on the right (secondary), joined by a strand, and a second strand rises from the secondary one. The principal oil cluster is less homogeneous, and changes in thickness are abrupt, while in the other core, these changes are gradual. Most spectral indices reveal an area of oil accumulation as a white filament in the left area of the image. It is dark in the NDVI but blends into the background in the CHL.

TABLE IV
ERROR METRICS FOR ASSESSING SPECTRAL INDICES

Index	Accuracy	Accuracy IQR	Oil F1-score	Water F1-score	γ
NDOI	0.945	**0.044**	0.830	0.961	**0.816**
Ratio B_2/B_{11}	0.921	0.079	**0.832**	0.948	0.808
RAI	0.940	0.054	0.812	0.957	0.797
NDVI	0.931	0.072	0.786	0.950	0.770
FI	**0.955**	0.060	0.779	**0.968**	0.768
NDWI	0.893	0.103	0.734	0.933	0.702
CDOM	0.870	0.140	0.711	0.881	0.702
WAF	0.882	0.116	0.710	0.926	0.677
OSI	0.865	0.056	0.618	0.894	0.593
CHL	0.862	0.082	0.601	0.896	0.578
HI	0.831	0.142	0.550	0.895	0.510

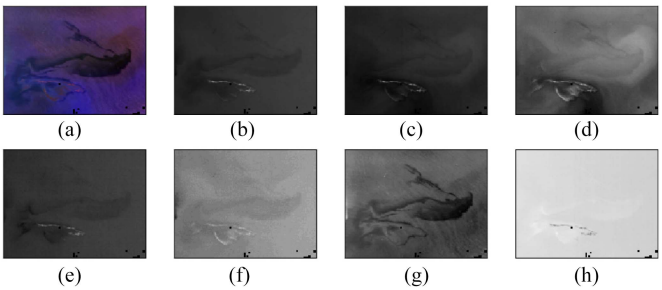

Fig. 11. MERIS false color RGB and spectral indices from 26 April 2010, at 15:58. (a) RGB MERIS 1. (b) NDOI. (c) RAI. (d) FI. (e) OSI. (f) CDOM. (g) CHL. (h) NDVI.

This behavior is probably a consequence of the solar illumination and oil thickness and causes the rest of the image to lose contrast. NDOI, RAI, and CDOM all show the entire silhouette of the spill, with NDOI being the clearest. In RAI, the second core has a lighter film around it, probably produced by sheens. These can be seen more clearly in FI, obstructing the distinction of the main spill. In OSI, the principal accumulation stands out more than the other one. NDVI shows a similar phenomenon, but in that case, it is more challenging to observe because of the stark contrast of the image with the highlighted filament. Finally, CHL has a different pattern from the rest. The right cluster is distinguishable, and the other has many undetected gaps. However, the overall silhouette is still distinguishable.

Fig. 12 shows the effect of masking this filament. The image contrast has improved, and the human eye perceives some spectral indices better. For example, in NDOI and NDVI, it is now possible to appreciate in more detail the spillage. Furthermore, the index indicates changes in spill thickness. This is a purely visual effect of facilitating interpretation, as the pixel values have not changed.

In conclusion, the thorough analysis of spectral indices from AVIRIS, HICO, and MERIS imagery has provided valuable insights into detecting and characterizing oil spills. This study reveals notable similarities and distinctions in the response of the spectral indices across different sensors and varying spill thicknesses. Challenges inherent in specific sensors, such as the absence of shortwave infrared range in HICO and MERIS, underscore the importance of careful selection and understanding of sensor capabilities for accurate oil spill assessment. It is worth noting that a supplementary spectral analysis of AVIRIS 2, HICO 2, and MERIS 2 is presented in the Appendix, further contributing to the comprehensive understanding of oil spill detection. This qualitative exploration sets the stage for a subsequent quantitative study.

C. NDOI Quantitative Analysis

In addition to the visual analysis, a quantitative analysis of the spectral indices is necessary. For this purpose, we present the confusion matrices, the accuracy, and the F1-score.

Fig. 13 shows the normalized confusion matrices corresponding to the NDOI indices applied to the six spectral images. Most matrices are very close to the identity, thus, indicating the effectiveness of the spectral index, except for the AVIRIS 2 and the HICO 2 matrices. This is because there is almost no coarse spillage in the scenes, and the index cannot distinguish it. The remaining confusion matrices have reasonably high hit rates, exceeding 95% success rate, which is desirable for good quality indices. In some cases, even the totality of the water pixels is correctly classified. Generally, for all images, the precision obtained by the oil class is higher than its recall. The quality of the pixels classified as oil is high, but the number of pixels identified is lower.

The median accuracy and F1-score values for the oil and water classes, as well as the interquartile range (IQR) of the accuracy and γ for each spectral index, are presented in Table IV. The best performance for each metric is in bold. NDOI presents a good compromise among all these values, showing promising results. It has very high accuracy (0.945) along with FI (0.955) and RAI (0.940). Moreover, NDOI is the most compact index, as indicated by its low IQR—noting its robustness. However, accuracy can be misleading when evaluating spectral indices; classes are unbalanced when detecting oil slicks in the vast sea. Therefore, a very accurate result can be obtained associated with a high hit rate for the water class, independently of the hit rate of the oil class. To better understand the indices' performance in

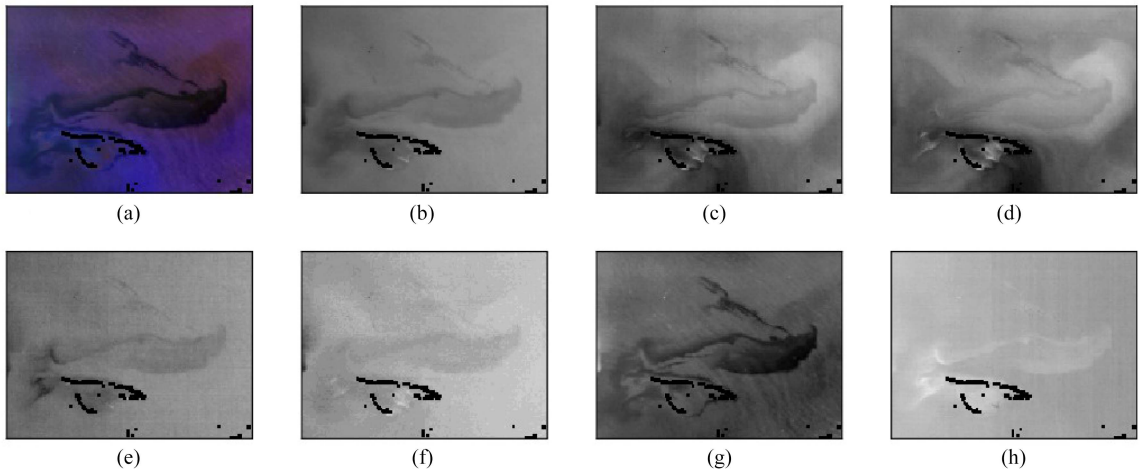

Fig. 12. MERIS false color RGB and spectral indices with masked glints from 26 April 2010, at 15:58. (a) RGB MERIS 1. (b) NDOI. (c) RAI. (d) FI. (e) OSI. (f) CDOM. (g) CHL. (h) NDVI.

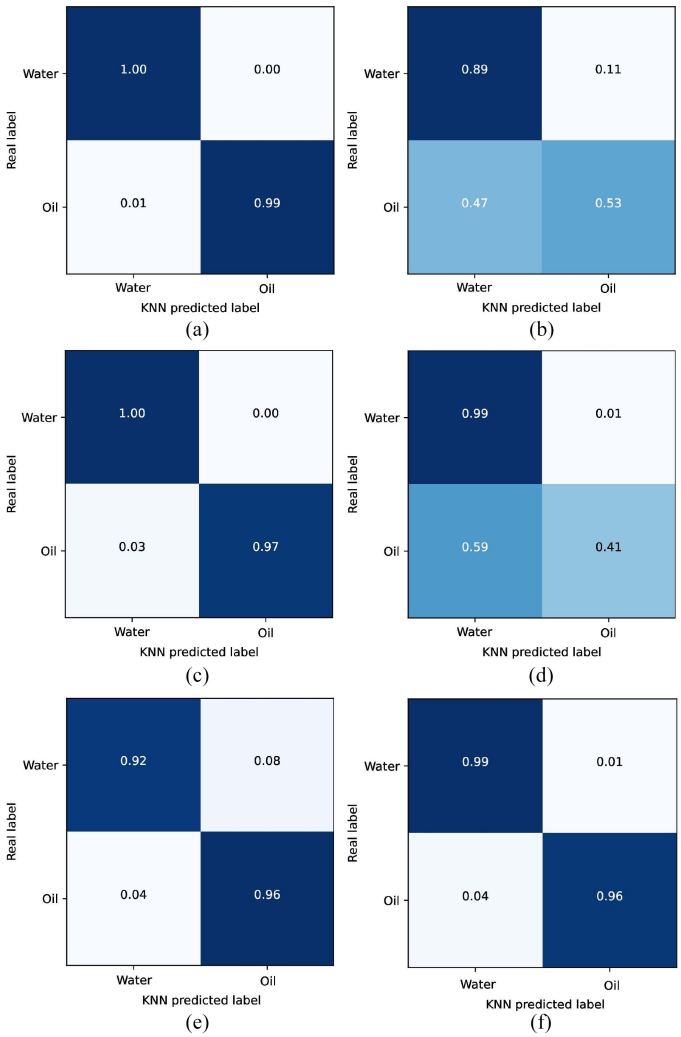

Fig. 13. Normalized confusion matrices of the NDOI spectral index for all spectral images. (a) AVIRIS 1. (b) AVIRIS 2. (c) HICO 1. (d) HICO 2. (e) MERIS 1. (f) MERIS 2.

detecting oil, we have examined the F1-score. This metric gives more importance to smaller classes, becoming more reliable in unbalanced situations. NDOI presents a water F1-score (0.961) that is very close to FI (0.968) and above RAI (0.957). But more relevant for our study, it has the second highest oil F1-score (0.830), which is the element that we want to monitor. NDOI oil F1-score value is after the B2/B11 ratio (0.832), followed by RAI (0.812). Lastly, NDOI shows the best result for γ (0.816), followed by ratio B2/B11 (0.808) and RAI (0.797). Acknowledging the potential bias in the results due to the inability to apply B2/B11, NDWI, HI, and WAF indices to HICO and MERIS is indispensable. The results in the overall accuracy of the best indices—FI, NDOI and RAI—are competitive with those obtained by AI techniques in similar oil spill studies. An accuracy of around 95% is attained with Random Forest (RF) and NN, and higher for support vector machine (SVM) operating directly on hyperspectral features and convolutional NNs [25].

In light of the above, NDOI has the best overall evaluation, as it has the second-best result in several metrics and the best in accuracy IQR and γ. In addition, the best value in the rest of the metrics does not correspond to a specific index but to several. RAI also has a very positive overall assessment, as it has obtained the third-best value in almost all metrics. However, the arithmetic operations involved in RAI calculation are computationally more expensive than in NDOI.

D. Thickness and Volume Differentiation

In this last section, the ability of NDOI to detect different thicknesses of spillage and volumes of oil is analyzed (see Fig. 14). For this purpose, two previous works will be taken as a reference [20], [45], where the authors estimate the thickness and oil volume with AVIRIS and MERIS imagery on dates very similar to those used in this work. Hence, the pixels for the training and test datasets are labeled using the outcomes of the studies as the ground truth. As already mentioned, the Bonn Agreement Oil

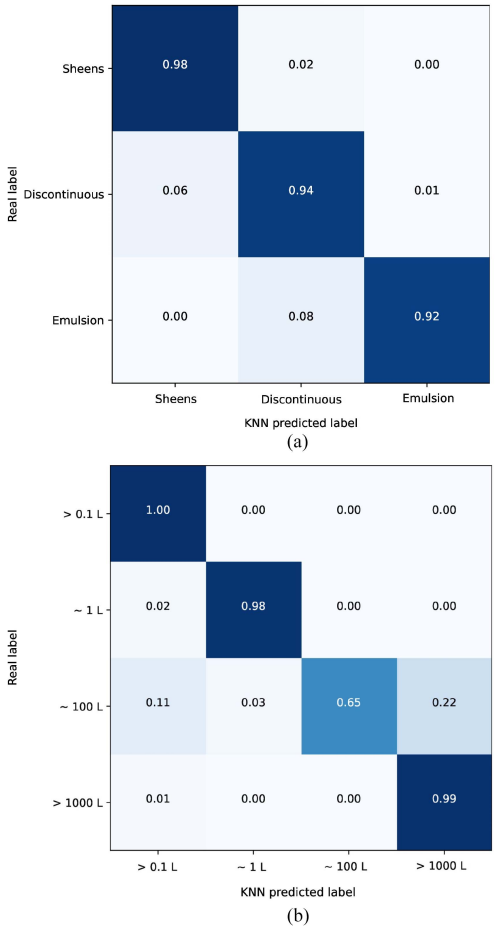

Fig. 14. Normalized confusion matrix of (a) spill thickness and of (b) the volume in liters of oil. (a) Thickness. (b) Volume.

Appearance Code has been adopted in this work to describe oil spills. Considering that the finer parts of the discharge evaporate quickly—those appearing silver, rainbow, and metallic, i.e., the part of the spill thinner than 50 microns—shall be grouped into one category called sheens. Four classes are distinguished: sheens (0.04–50 microns), discontinuous true-color oil (50–200 microns), continuous true-color (>200 microns), and emulsion (>500 microns).

Based on the research by Zhao et al. [45], it is possible to distinguish between three types of oil slicks: sheens, discontinuous true-color oil, and emulsions in AVIRIS 1. However, continuous true-color oil could not be identified, as it is mistaken for discontinuous true-color oil, as could already be guessed from the visual analysis. Denser parts of the spill have different spectral behavior. As shown in Fig. 14, most of the sheen pixels are qualified as such using NDOI. Nevertheless, NDOI misclassifies some discontinuous oil pixels as sheen pixels and assigns some emulsion pixels to the discontinuous oil class. Again, the algorithm obtains higher precision than recall for all categories. F1-score results for sheen, discontinuous true-color oil, and emulsion classes are satisfactory, with 0.977, 0.944, and 0.946, respectively, and an overall accuracy of 0.964 and an F1-score of 0.955.

Hu et al. [20] carried out the second work, where they calculated the oil volume of the spill with MERIS images. Although there are no images of the exact date, the difference is only two days with MERIS 2. As the work covered the complete spill, we estimate that the variations in the volume are not significant in this period, and the article results serve as a reference for us. The success rate of the classes using NDOI is very high (above 95%) except for a volume of about 100 L, which is easily confused with the regions of around 1000 L (65%). The F1-score for the classes from less than 1 L to more than 1000 L is 0.990, 0.987, 0.787, and 0.985, correspondingly, resulting in an overall F1-score of 0.937 and an overall accuracy of 0.985.

Considering that the preceding metrics give very satisfactory results, above 90% in all cases, we consider that NDOI can distinguish between different thicknesses of the spill and among oil volumes. Based on the replication of prior research results, the index's performance has overcome the effect of sunglint and the optical complexity of analyzing the entire spot. Moreover, AI techniques excel in the differentiation of oil thicknesses at the cost of increased computational time [25]. Spectral indices are thus a safe bet for studies using satellites or airborne sensors.

V. Conclusion

NDOI has proven to be effective when applied to different sensor data. It accentuates contaminated parts of medium and high thickness, although it is more challenging to identify sheens and very dense spots where the oil is almost black. With NDOI, we have detected the complete oil spill, with all the difficulties that this entails, and different thicknesses have been identified in several scenes. Its performance on all images is comparable to other indices in the literature, such as FI, CDOM, and NDVI, and is remarkably consistent with RAI. Its main advantage over the other indices is that it does not misclassify the sand in suspension from the Mississippi River delta and the spill. This can be a significant improvement when studying coastal spills. The fewer oil slick look-alikes that can occur, the less likely false spill detection will happen. Another great advantage of NDOI is that the bands used are ubiquitous in optical sensors, and it does not need to cover the infrared range, thus making its applicability wider. Regarding the performance quality, the oil hit rate exceeds 95% in all images with coarse spillage, reaching an average accuracy of 0.945 and an average F1-score of 0.830. Consequently, NDOI achieves the highest overall rating among the spectral indices, with a figure of merit that combines accuracy and F1-score (0.816). In addition, even under the sunglint effect, it has been possible to reproduce the literature estimate of spill thickness and oil volume with metrics results exceeding 90%.

NDOI is more than adequate for detecting spills with thicknesses more significant than 50 microns. It utilizes universal bands in satellites, and due to its ease of use and quick calculation time, its incorporation in hardware acceleration devices is also appropriate, reducing the processing time, the resources needed, and the energy consumed. At a further stage of our research, the efficiency of NDOI on other spills will be assessed, along with the potential for misclassification with other oil slick look-alikes. We have also started to develop low-cost sensors with bands

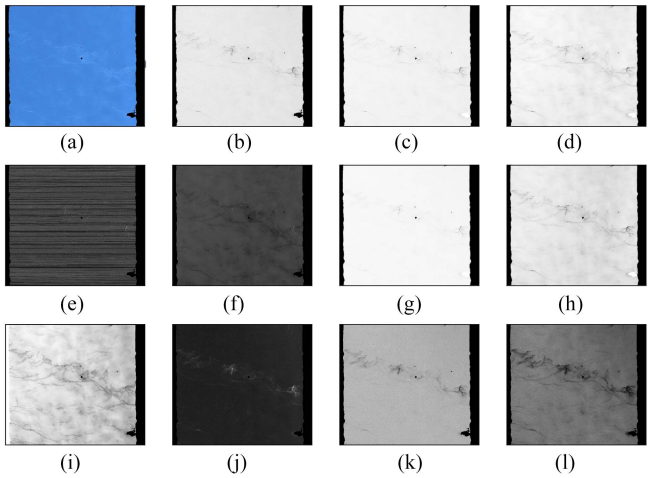

Fig. 15. AVIRIS true color RGB and spectral indices from 18 May 2010, at 19:59. (a) RGB AVIRIS 2. (b) NDOI. (c) RAI. (d) FI. (e) HI. (f) OSI. (g) WAF. (h) CDOM. (i) CHL. (j) NDVI. (k) NDWI. (l) RATIO B2/B11.

tailored to the specific requirements of particular scenarios. The combination of low-cost multispectral sensors and UAVs allows us to respond quickly to environmental crises and minimize their impact. Implementing multispectral sensors with the required wavelengths to obtain NDOI will allow real-time results, further facilitating decision-making in critical situations.

Appendix
Extension of the Qualitative Analysis

The qualitative analysis of these images is complementary to the investigations conducted in Section IV-B. It enhances our understanding by providing nuanced insights and a visual perspective of AVIRIS 2, HICO 2, and MERIS 2.

AVIRIS 2 (see Fig. 15), taken the following day of AVIRIS 1, shows similar behavior to that already observed. In this scene, the spill is not very thick. The RGB image shows how some low-thickness filaments, perhaps mixed with water, cross the image horizontally. Around them, there is some sheen coming from thin layers of oil. The NDOI, RAI, FI, and CDOM indices highlight the few regions of thicker contamination in the image— which is more noticeable in CDOM. Analogously, the NDVI emphasizes the same pattern but reversed. Once again, the index that most reveals the fine contamination is the B2/B11 ratio, as the shape of the spill is visible, and some sheens are discernible. On this occasion, neither HI nor OSI can be accepted as valid indices. In this scene, the HI banding obstructs the analysis of the image. Part of the spill is visible in OSI, but the difference between oil and water is not evident. Similar issues arise with CHL, where the thin crude oil film can be better distinguished. However, the separation between the sea and the sheen is still hazy, blurring the result and making interpretation difficult. The WAF result is essentially nonexistent because there is no thick film in the scene except for a few minor soft spots. Finally, despite the lack of sheens, the NDWI can still make out the narrow bands of spills.

HICO 2, represented in Fig. 16, has similar characteristics to AVIRIS 2. It is a scene with clouds in which only thin patches are found. Consequently, the behavior of the spectral indices is likely

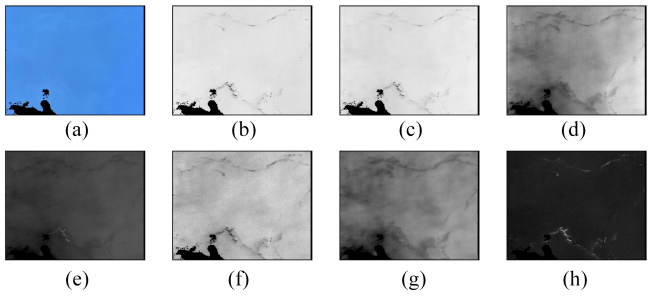

Fig. 16. HICO false color RGB and spectral indices from 28 May 2010, at 13:21. (a) RGB HICO 2. (b) NDOI. (c) RAI. (d) FI. (e) OSI. (f) CDOM. (g) CHL. (h) NDVI.

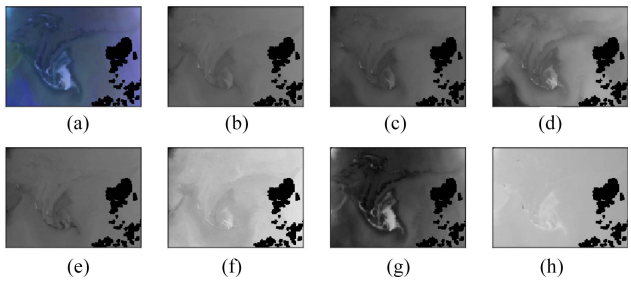

Fig. 17. MERIS false color RGB and spectral indices from 2 May 2010, at 03:51. (a) RGB MERIS 2. (b) NDOI. (c) RAI. (d) FI. (e) OSI. (f) CDOM. (g) CHL. (h) NDVI.

to be similar as well. NDOI and RAI are visually identical, indicating the regions of fuel accumulation. The NDVI reproduces this same behavior. CDOM, as on previous occasions, highlights the thicker areas of the spill and some thinner parts. FI and CHL enhance its fine details even more, reaching a situation where it is difficult to distinguish the main spill path. Likewise, we identify the area with the highest accumulation with OSI, but the distinction with the less polluted area is blurred.

MERIS 2 presents a similar situation to MERIS 1 (see Fig. 17). The spill is complex and shows significant variations in spectral behavior. At first glance, CHL indicates all the core characteristics and upper ridges. Next is FI, which outlines the silhouette of the spill and gives a glimpse of the crests. In RAI and NDOI, it is more difficult to distinguish the peaks from the background. OSI, CDOM, or NDVI cannot accurately detect ridges. However, the core is visible in all three indices, and it is easy to identify with OSI.

References

[1] G. Andreoli, B. Bulgarelli, B. Hosgood, and D. Tarchi, "Hyperspectral analysis of oil and oil-impacted soils for remote sensing purposes," *Eur. Commission Joint Res. Centre: Luxembourg*, vol. 36, pp. 2–30, 2007.

[2] D. Angelova, I. Uzunov, S. Uzunova, A. Gigova, and L. Minchev, "Kinetics of oil and oil products adsorption by carbonized rice husks," *Chem. Eng. J.*, vol. 172, no. 1, pp. 306–311, 2011. [Online]. Available: https://www.sciencedirect.com/science/article/pii/S1385894711006954

[3] M. Fingas and C. Brown, "Review of oil spill remote sensing," *Mar. Pollut. Bull.*, vol. 83, no. 1, pp. 9–23, 2014. [Online]. Available: https://www.sciencedirect.com/science/article/pii/S0025326X14002021

[4] M. Fingas and C. Brown, "Chapter 5–oil spill remote sensing," in *Oil Spill Science and Technology*, 2nd ed., M. Fingas, Ed. Amsterdam, The Netherlands: Elsevier, 2017, pp. 305–385.

[5] C. Brekke and A. H. Solberg, "Oil spill detection by satellite remote sensing," *Remote Sens. Environ.*, vol. 95, no. 1, pp. 1–13, 2005. [Online]. Available: https://www.sciencedirect.com/science/article/pii/S0034425704003724

[6] P. Odonkor, Z. Ball, and S. Chowdhury, "Distributed operation of collaborating unmanned aerial vehicles for time-sensitive oil spill mapping," *Swarm Evol. Comput.*, vol. 46, pp. 52–68, 2019. [Online]. Available: https://www.sciencedirect.com/science/article/pii/S2210650217309288

[7] N. Aghaei, G. Akbarizadeh, and A. Kosarian, "Osdes_net: Oil spill detection based on efficient_shuffle network using synthetic aperture radar imagery," *Geocarto Int.*, vol. 37, no. 26, pp. 13539–13560, 2022.

[8] J. L. E. Honrado, D. B. Solpico, C. M. Favila, E. Tongson, G. L. Tangonan, and N. J. C. Libatique, "UAV imaging with low-cost multispectral imaging system for precision agriculture applications," in *Proc. IEEE Glob. Humanitarian Technol. Conf.*, 2017, pp. 1–7.

[9] A. Morales et al., "A multispectral camera development: From the prototype assembly until its use in a UAV system," *Sensors*, vol. 20, no. 21, 2020, Art. no. 6129. [Online]. Available: https://www.mdpi.com/1424-8220/20/21/6129

[10] A. Pérez-García, A. Rodríguez-Molina, E. Hernández, L. Vera, and J. F. López, "Development of low-cost multi-spectral cameras for precision agriculture," in *Proc. IEEE Int. Geosci. Remote Sens. Symp.*, 2023, pp. 3466–3469.

[11] V. Satriano, E. Ciancia, T. Lacava, N. Pergola, and V. Tramutoli, "Improving the RST-oil algorithm for oil spill detection under severe sun glint conditions," *Remote Sens.*, vol. 11, no. 23, 2019, Art. no. 2762. [Online]. Available: https://www.mdpi.com/2072-4292/11/23/2762

[12] C. R. Jackson and W. Alpers, "The role of the critical angle in brightness reversals on sunglint images of the sea surface," *J. Geophysical Research: Oceans*, vol. 115, no. C9, 2010, Art. no. C09019.

[13] M. Fingas and C. E. Brown, "A review of oil spill remote sensing," *Sensors*, vol. 18, no. 91, pp. 1–18, 2018. [Online]. Available: https://www.mdpi.com/1424-8220/18/1/91

[14] J. Zhao, M. Temimi, H. Ghedira, and C. Hu, "Exploring the potential of optical remote sensing for oil spill detection in shallow coastal waters-a case study in the arabian gulf," *Opt. Exp.*, vol. 22, no. 11, pp. 13755–13772, Jun. 2014. [Online]. Available: http://www.opticsexpress.org/abstract.cfm?URI=oe-22-11-13755

[15] A. J. Brown, "Spectral curve fitting for automatic hyperspectral data analysis," *IEEE Trans. Geosci. Remote Sens.*, vol. 44, no. 6, pp. 1601–1608, Jun. 2006.

[16] J. Yang, J. Wan, Y. Ma, J. Zhang, and Y. Hu, "Characterization analysis and identification of common marine oil spill types using hyperspectral remote sensing," *Int. J. Remote Sens.*, vol. 41, no. 18, pp. 7163–7185, 2020, doi: 10.1080/01431161.2020.1754496.

[17] M. Fingas, "Visual appearance of oil on the sea," *J. Mar. Sci. Eng.*, vol. 9, no. 97, pp. 1–13, 2021.

[18] R. N. Clark et al., "A method for quantitative mapping of thick oil spills using imaging spectroscopy," *US Geological Surv. Open-File Rep.*, vol. 1167, no. 2010, pp. 1–51, 2010.

[19] J. Svejkovsky, M. Hess, J. Muskat, T. J. Nedwed, J. McCall, and O. Garcia, "Characterization of surface oil thickness distribution patterns observed during the deepwater horizon (MC-252) oil spill with aerial and satellite remote sensing," *Mar. Pollut. Bull.*, vol. 110, no. 1, pp. 162–176, 2016.

[20] C. Hu et al., "Remote sensing estimation of surface oil volume during the 2010 deepwater horizon oil blowout in the gulf of Mexico: Scaling up AVIRIS observations with MODIS measurements," *J. Appl. Remote Sens.*, vol. 12, no. 2, pp. 1–44, 2018, doi: 10.1117/1.JRS.12.026008.

[21] L. Xu, J. Li, and A. Brenning, "A comparative study of different classification techniques for marine oil spill identification using radarsat-1 imagery," *Remote Sens. Environ.*, vol. 141, pp. 14–23, 2014. [Online]. Available: https://www.sciencedirect.com/science/article/pii/S0034425713003805

[22] A. Raeisi, G. Akbarizadeh, and A. Mahmoudi, "Combined method of an efficient cuckoo search algorithm and nonnegative matrix factorization of different zernike moment features for discrimination between oil spills and lookalikes in SAR images," *IEEE J. Sel. Topics Appl. Earth Observ. Remote Sens.*, vol. 11, no. 11, pp. 4193–4205, Nov. 2018.

[23] F. M. Ghara, S. B. Shokouhi, and G. Akbarizadeh, "A new technique for segmentation of the oil spills from synthetic-aperture radar images using convolutional neural network," *IEEE J. Sel. Topics Appl. Earth Observ. Remote Sens.*, vol. 15, pp. 8834–8844, 2022.

[24] R. Al-Ruzouq et al., "Sensors, features, and machine learning for oil spill detection and monitoring: A review," *Remote Sens.*, vol. 12, no. 20, 2020, Art. no. 3338. [Online]. Available: https://www.mdpi.com/2072-4292/12/20/3338

[25] B. Wang et al., "A spectral-spatial features integrated network for hyperspectral detection of marine oil spill," *Remote Sens.*, vol. 13, no. 8, 2021, Art. no. 1568. [Online]. Available: https://www.mdpi.com/2072-4292/13/8/1568

[26] Z. Xiao, S. Liang, J. Wang, B. Jiang, and X. Li, "Real-time retrieval of leaf area index from modis time series data," *Remote Sens. Environ.*, vol. 115, no. 1, pp. 97–106, 2011. [Online]. Available: https://www.sciencedirect.com/science/article/pii/S003442571000249X

[27] Y. Liu, A. MacFadyen, Z.-G. Ji, and R. H. Weisberg, "Introduction to monitoring and modeling the deepwater horizon oil spill," *Geophys. Monogr. Ser*, vol. 195, pp. 1–7, 2011.

[28] O. Garcia-Pineda et al., "Detection of oil near shorelines during the deepwater horizon oil spill using synthetic aperture radar (SAR)," *Remote Sens.*, vol. 9, no. 6, 2017, Art. no. 567. [Online]. Available: https://www.mdpi.com/2072-4292/9/6/567

[29] A. Pérez-García, P. Horstrand, and J. F. López, "Ndoi, a novel oil spectral index: Comparisons and results," in *Proc. 12th Workshop Hyperspectral Imag. Signal Process.: Evol. Remote Sens.*, 2022, pp. 1–5.

[30] N. Audebert, B. L. Saux, and S. Lefèvre, "Deep learning for classification of hyperspectral data: A comparative review," *IEEE Geosci. Remote Sens. Mag.*, vol. 7, no. 2, pp. 159–173, Jun. 2019.

[31] S. Hafeez et al., "Detection and monitoring of marine pollution using remote sensing technologies," in *Monitoring of Marine Pollution* (ser. Chapters), H. B. Fouzia, Ed. London, U.K.: IntechOpen, Sep. 2019. [Online]. Available: https://ideas.repec.org/h/ito/pchaps/163515.html

[32] I. Leifer et al., "State of the art satellite and airborne marine oil spill remote sensing: Application to the bp deepwater horizon oil spill," *Remote Sens. Environ.*, vol. 124, pp. 185–209, 2012. [Online]. Available: https://www.sciencedirect.com/science/article/pii/S0034425712001563

[33] B. Zhang, L. Zhao, and X. Zhang, "Three-dimensional convolutional neural network model for tree species classification using airborne hyperspectral images," *Remote Sens. Environ.*, vol. 247, 2020, Art. no. 111938. [Online]. Available: https://www.sciencedirect.com/science/article/pii/S0034425720303084

[34] T. Bijeesh and K. Narasimhamurthy, "A comparative study of spectral indices for surface water delineation using landsat 8 images," in *Proc. Int. Conf. Data Sci. Commun.*, IEEE, 2019, pp. 1–5.

[35] A. Pérez-García, P. Horstrand, and J. F. López, "A novel spectral index for ocean oil spill detection," in *Proc. ESA Living Planet Symp.*, 2022, p. 1.

[36] E. Loos, L. Brown, G. Borstad, T. Mudge, and M. Álvarez, "Characterization of oil slicks at sea using remote sensing techniques," in *Proc. Oceans*, IEEE, 2012 pp. 1–4.

[37] F. K. C. author, K. Oppermann, and B. Hörig, "Hydrocarbon index–An algorithm for hyperspectral detection of hydrocarbons," *Int. J. Remote Sens.*, vol. 25, no. 12, pp. 2467–2473, 2004, doi: 10.1080/01431160310001642287.

[38] Q. Li, L. Lu, B. Zhang, and Q. Tong, "Oil slope index: An algorithm for crude oil spill detection with imaging spectroscopy," in *Proc. 2nd Int. Workshop Earth Observ. Remote Sens. Appl.*, 2012, pp. 46–49.

[39] W.-Z. Lu et al., "Modern near infrared spectroscopy analytical technology," 2nd ed. *Beijing: China Petrochemical Press*, 2007.

[40] T. Kutser, D. C. Pierson, K. Y. Kallio, A. Reinart, and S. Sobek, "Mapping lake CDOM by satellite remote sensing," *Remote Sens. Environ.*, vol. 94, no. 4, pp. 535–540, 2005. [Online]. Available: https://www.sciencedirect.com/science/article/pii/S0034425704003670

[41] C. Hu, Z. Lee, and B. Franz, "Chlorophyll algorithms for oligotrophic oceans: A novel approach based on three-band reflectance difference," *J. Geophysical Res.: Oceans*, vol. 117, no. C1, 2012, Art. no. C01011.

[42] D. A. Carlson and T. N. Ripley, "On the relation between NDVI, fractional vegetation cover, and leaf area index," *Remote Sens. Environ.*, vol. 62, no. 3, pp. 241–252, 1997.

[43] B. cai Gao, "NDWI–A normalized difference water index for remote sensing of vegetation liquid water from space," *Remote Sens. Environ.*, vol. 58, no. 3, pp. 257–266, 1996. [Online]. Available: https://www.sciencedirect.com/science/article/pii/S0034425796000673

[44] P. Kolokoussis and V. Karathanassi, "Oil spill detection and mapping using sentinel 2 imagery," *J. Mar. Sci. Eng.*, vol. 6, no. 4, pp. 1–12, 2018. [Online]. Available: https://www.mdpi.com/2077-1312/6/1/4

[45] D. Zhao, X. Cheng, H. Zhang, Y. Niu, Y. Qi, and H. Zhang, "Evaluation of the ability of spectral indices of hydrocarbons and seawater for identifying oil slicks utilizing hyperspectral images," *Remote Sens.*, vol. 10, no. 3, 2018, Art. no. 421. [Online]. Available: https://www.mdpi.com/2072-4292/10/3/421

[46] V. Klemas, "Tracking oil slicks and predicting their trajectories using remote sensors and models: Case studies of the sea princess and deepwater horizon oil spills," *J. Coastal Res.*, vol. 2010, no. 265, pp. 789–797, 2010, doi: 10.2112/10A-00012.1.
[47] L. Cong, B. Nutter, and D. Liang, "Estimation of oil thickness and aging from hyperspectral signature," in *2012 IEEE Southwest Symp. Image Anal. Interpretation*, 2012, pp. 213–216.
[48] V. Karathanassi, "Spectral unmixing evaluation for oil spill characterization," *Int. J. Remote Sens. Appl.*, vol. 4, pp. 1–17, 2014.
[49] F. Carnesecchi, V. Byfield, P. Cipollini, G. Corsini, and M. Diani, "An optical model for the interpretation of remotely sensed multispectral images of oil spill," *Proc. SPIE*, vol. 7105, pp. 11–22, 2008, doi: 10.1117/12.800304.
[50] A. K. Mishra and G. S. Kumar, "Weathering of oil spill: Modeling and analysis," *Aquatic Procedia*, vol. 4, pp. 435–442, 2015, International Conference on Water Resources, Coastal and Ocean Engineering. [Online]. Available: https://doi.org/10.1016/j.aqpro.2015.02.058
[51] B. Agreement, "Bonn agreement website," 2024. [Online]. Available: https://www.bonnagreement.org/
[52] R. O. Green et al., "Imaging spectroscopy and the airborne visible/infrared imaging spectrometer (aviris)," *Remote Sens. Environ.*, vol. 65, no. 3, pp. 227–248, 1998.
[53] N. Jet Propulsion Laboratory, "Airbone visible infrared imaging spectrometer website," 2021. [Online]. Available: https://aviris.jpl.nasa.gov/
[54] NASA, "Earth data, oceancolor web, HICO," 2021. [Online]. Available: https://oceancolor.gsfc.nasa.gov/data/hico/
[55] E. S. A. Signature, "Earth online, envisat, meris," 2021. [Online]. Available: https://earth.esa.int/eogateway/instruments/meris
[56] Y. Mo, M. S. Kearney, and J. C. A. Riter, "Post-deepwater horizon oil spill monitoring of louisiana salt marshes using landsat imagery," *Remote Sens.*, vol. 9, no. 6, 2017, Art. no. 547. [Online]. Available: https://www.mdpi.com/2072-4292/9/6/547
[57] L. Gómez-Chova, G. Camps-Valls, J. Calpe-Maravilla, L. Guanter, and J. Moreno, "Cloud-screening algorithm for ENVISAT/MERIS multispectral images," *IEEE Trans. Geosci. Remote Sens.*, vol. 45, no. 12, pp. 4105–4118, Dec. 2007.
[58] E. Fix and J. L. Hodges, "Discriminatory analysis: Nonparametric discrimination: Consistency properties," *Int. Stat. Rev./Revue Int. de Statistique*, vol. 57, no. 3, pp. 238–247, 1989.
[59] N. S. Altman, "An introduction to kernel and nearest-neighbor nonparametric regression," *Amer. Statist.*, vol. 46, no. 3, pp. 175–185, 1992. [Online]. Available: https://www.tandfonline.com/doi/abs/10.1080/00031305.1992.10475879
[60] I. Mani and I. Zhang, "kNN approach to unbalanced data distributions: A case study involving information extraction," in *Proc. Workshop Learn. Imbalanced Datasets*, 2003, vol. 126, pp. 1–7.
[61] M. Hossin and M. N. Sulaiman, "A review on evaluation metrics for data classification evaluations," *Int. J. Data Mining Knowl. Manage. Process*, vol. 5, no. 2, pp. 1–11, 2015.
[62] S. Boughorbel, F. Jarray, and M. El-Anbari, "Optimal classifier for imbalanced data using Matthews correlation coefficient metric," *PLoS One*, vol. 12, no. 6, 2017, Art. no. e0177678.

Ámbar Pérez-García (Graduate Student Member, IEEE) was born in Las Palmas de Gran Canaria, Spain, in 1997. She received the B.Sc. degree in physics from the University of La Laguna (ULL), La Laguna, Spain, and the M.Sc. degree in remote sensing from the University of Valencia (UV), Valencia, Spain, in 2019 and 2020, respectively, the M.Sc. degree in education from the University of La Rioja (UNIR), La Rioja, Spain, in 2021. She is currently working toward the Ph.D. degree in telecommunications technologies with the University of Las Palmas de Gran Canaria (ULPGC), Las Palmas de Gran Canaria, Spain.

She is with the Institute for Applied Microelectronics, IUMA, University of Las Palmas de Gran Canaria, Las Palmas de Gran Canaria, Spain. In 2023, she did a research stay on neural network segmentation with HYPERCOMP, University of Extremadura, Spain. She was also with HWM, Wageningen University & Research, The Netherlands, spectrally characterizing plastics. Her research interests include remote sensing, hyperspectral image processing, artificial intelligence, and the detection of marine litter.

Adrián Rodríguez-Molina was born in Las Palmas de Gran Canaria, Spain, in 1998. He received the engineering degree in industrial electronics and automatic from the University of Las Palmas de Gran Canaria, Las Palmas de Gran Canaria, Spain, in 2020, and the master's degree in applied electronics and telecommunications from the Institute for Applied Microelectronics, Las Palmas de Gran Canaria, Spain, in 2021. He is currently working toward the Ph.D. degree in telecommunication technologies and computational engineering with the University of Las Palmas de Gran Canaria (ULPGC), developing a multipurpose multispectral camera with built-in artificial intelligence.

Emma Hernández was born in Las Palmas de Gran Canaria in 1997. She received the bachelor's degree in industrial and automatic electronic engineering from the University of Las Palmas de Gran Canaria (ULPGC), Las Palmas de Gran Canaria, Spain, and the master's degree in control and robotics from the Polytechnic University of Madrid (UPM), Madrid, Spain, in 2020 and 2021, respectively. She is currently working toward the Ph.D. degree in telecommunications technologies with the ULPGC.

She is a Researcher with the Institute of Applied Microelectronics, IUMA, University of Las Palmas de Gran Canaria, Las Palmas de Gran Canaria, Spain. In 2023, she conducted a research stay in thermographic image processing at the University of Oviedo, Spain. Her research interests include image processing, unmanned aerial vehicles (UAVs), hyperspectral technology, and thermography technologies and their applications.

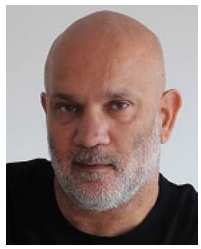

José Fco López received the M.S. degree in physics (specializing in electronics) from the University of Seville, Sevilla, Spain, in 1989 and the Ph.D. degree in high-speed integrated systems from the University of Las Palmas de Gran Canaria (ULPGC), Las Palmas de Gran Canaria, Spain, in 1994.

He was with Thomson Composants Microondes, Orsay, France, in 1992. In 1995, he was with the Center for Broadband Telecommunications, Technical University of Denmark (DTU), Lyngby, Denmark. In 1996, 1997, 1999, and 2000, he was a Visiting Researcher with the Edith Cowan University (ECU), Perth, Western Australia. He has conducted investigations with the Institute for Applied Microelectronics (IUMA), where he has acted as Deputy Director since 2009. He is currently a Lecturer with the School of Telecommunication and Electronics Engineering and with an M.Sc. Program of IUMA, ULPGC. He has authored/coauthored around 150 papers in national and international journals and conferences. His current research interests include image processing, UAVs, hyperspectral technology, and their applications.

Dr López has been actively enrolled in more than 50 research projects funded by the European Community, Spanish Government, and international private industries in Europe, the USA, and Australia.